Numerical evaluation of micro-structural parameters of porous supports in metal-supported solid oxide fuel cells

Georg Reiss [a], *, Henrik Lund Frandsen [b], Wilhelm Brandstätter [c], André Weber [d]

[a] ICE Strömungsforschung GmbH, Hauptplatz 13, 8700 Leoben, Austria
[b] Technical University of Denmark, Department of Energy Storage and Conversion, Frederiksborgvej 399, 4000 Roskilde, Denmark
[c] Montanuniversität Leoben, Lehrstuhl für Petroleum and Geothermal Energy Recovery, Franz-Josef-Straße 18, 8700 Leoben, Austria
[d] Karlsruher Institut für Technologie (KIT), Institut für Werkstoffe der Elektrotechnik (IWE), Adenauerring 20b, D-76131 Karlsruhe, Germany

HIGHLIGHTS

- Improved method to determine averaged transport parameters e.g. porosity, tortuosity.
- Based on reconstruction of 3D micro-structures of a metal-supported SOFC.
- Correct lateral boundary conditions change state-of-the art approach with 47%.
- Assessment of anisotropic micro-structures by determining the porosity distribution.
- Transport parameters for different dense layers are computed separately.

ARTICLE INFO

ABSTRACT

Metallic supported Solid Oxide Fuel Cells (SOFCs) are considered as a durable and cost effective alternative to the state-of-the-art ceramic supported cell designs. In order to understand the mass and charge transport in the metal-support of this new type of cell a novel technique involving X-ray tomography and micro-structural modelling is presented in this work. The simulation technique comprises a novel treatment of the boundary conditions, which leads to more accurate effective transport parameters compared to those, which can be achieved with the conventional homogenisation procedures. Furthermore, the porosity distribution in the metal-support was determined, which provided information about the inhomogeneous nature of the material. In addition to that, transport parameters for two identified, different dense layers of the metal-support are evaluated separately.

The results of the evaluation show three significant findings. Firstly, that the effective transport parameters are up to a factor of 20 lower compared to other SOFC anodes. Secondly, that the micro-structure can have regions, which are much denser, especially the first 100 μm of the interface between gas-channel and support-structure. Thirdly, that the calculation of the transport parameters depends on the correct application of boundary conditions.

© 2014 Elsevier B.V. All rights reserved.

1. Introduction

The solid oxide fuel cell (SOFC) technology offers effective conversion of chemical stored energy to electricity. The state-of-the-art SOFC-stack is based mainly on all-ceramic cells, which are brittle and thus challenging to operate. During the operation of the SOFCs heat is generated, which must be transported out of the stack resulting in thermal gradients. These thermal gradients will cause thermal stresses, which may induce cracks in the ceramic cells. A second failure mechanism in state-of-the-art cells is the re-oxidation of the nickel/zirconia cermet anode and substrate. A re-oxidation of the nickel will result in a volume expansion and thus the formation of cracks. To overcome these drawbacks, alternative types of SOFCs based on porous metallic supports have been developed, exhibiting a number of advantages as an improved mechanical strength, a higher thermal conductivity of the substrate and a higher re-oxidation tolerance of the applied alloys. The actual cell and stack developments performed worldwide have shown very promising results compared to the state-of-the-art cells [1–9].

In order to avoid failures and optimise the cells further, experiments are carried out to study their behaviour [1,10], but the

* Corresponding author. Tel.: +43 3842 9828259; fax: +43 3842 9828212.
E-mail address: georg.reiss@ice-sf.at (G. Reiss).
URL: http://www.ice-sf.at

theoretical foundation to understand their behaviour must also be developed. To this end, multi-physics models describing the variety of physics are being developed see e.g. Refs. [11–13]. The physics involved are: electronic and ionic charge transfer; solid mechanics; heat transfer; gas diffusion and flow. The parameters used in these multi-physics models can either be measured or deducted by micro-structural modelling. The measurements are typical on the cell level, why a convoluted response is measured and the physically meaningful parameters can only be determined by a reverse engineering approach if an appropriate electro-chemical model is existing [14]. In addition to that, if a component is modified or a new component is developed all physical parameters have to be re-measured. Therefore, a novel route based on micro-structural modelling of the material parameters is pursued in this work.

The various physical phenomena occurring in a SOFC take place on a large span of length scales from sub-micron to centimetres. Thus, in order to obtain meaningful computational results, the material properties and the material structure of the SOFC under investigation have to be represented in detailed micro-structural models. However, a high spatial resolution of the electrode structure will result in a computational model containing a tremendous amount of mesh cells, and will thus lead to impractical calculation times. Calculations of an entire SOFC-stack (12 cm × 12 cm × 10 cm) with a resolution of 1 μm^3 would result in approx. 1×10^{15} computational cells, which would require memory capacities exceeding most of the available supercomputers.

Often the details occurring on smaller scales are indirectly included through the applied material models or so-called constitutive models, in which the material parameters are fitted to experimental results. With the many interacting physics in SOFC, the modelling entails a large number of unknown parameters. The combined response of the cell can to some degree be decoupled by electrochemical impedance spectroscopy and e.g. by controlling the gas composition on the anode and the cathode side, such that parameters related to phenomena occurring either side can be determined. However, the combined response is a convolution of all the parameters, which makes the fitting task quite difficult.

This was successfully performed and shown in Ref. [14] at elevated temperatures (>800 °C). However, at lower temperatures the gas diffusion process in the anode substrate is overlapped by a process related to the hydrogen electro-oxidation in the impedance spectra, and deconvolution is thus not possible. The cell studied in this work has limited stability at these temperatures, and thus so far it has not been possible to determine the mass transport resistance with electrochemical impedance spectroscopy. Alternatively, one of the processes, e.g. the gas diffusion, could be studied separately allowing for a better deconvolution of the overall response. It should, however, be noted that the deconvolution approach only allows for determining the integrated diffusion resistance of all layers on either side of the electrolyte. Thus, for a direct study of the implication of variation of the composition and thickness of the individual layers other methods must be applied. Furthermore, it is given that the usage of this measurement/fitting approach will only re-produce the experiments that they rely on, but the impact of variations of micro-structure or maybe even layer thicknesses requires new experiments. In the spirit of John von Neumann, a mathematician and computer scientist:

> With four parameters I can fit an elephant, and with five I can make him wiggle his trunk;

computational attempts to reduce the level of uncertainty about these parameters should be undertaken.

The possibility to analyse the micro-structure of the electrodes by e.g. focused ion beam – scanning electron microscope (FIB-SEM) or X-ray computed tomography (CT) has therefore lead to a number of modelling studies of the phenomena occurring on the micro-scale [15–21]. The established methodology is to apply FIB-SEM measurements for regions, where a high resolution is needed see e.g. Ref. [22]. Only a small part of the electrode can be investigated with this method, whereas CT-scanning can be used to analyse larger volumes of the micro-structure. Nevertheless, X-ray nano-tomography yields comparable results to FIB-SEM [23,24]. The two approaches compliment and overlap each other in their regime of use. Common for both is that the data obtained is a sequence of two dimensional pictures, which has to be transformed into a three-dimensional voxelised picture of the micro-structure. This is used to reconstruct a computational geometry, after image processing with an in-house algorithm based on [25–28]. Subsequently, effective transport properties are calculated using numerical models. This approach has been used a number of times for SOFC anodes and cathodes [15–21], but was, to the author's knowledge, not yet applied to the porous metal-support. The new technology of a metallic porous support for the SOFC implicates a change of the micro-structure due to corrosion during operation. This is a very important issue in the development of durable metal-supports and is object to many experiments [29–32]. While improving the stability of the cells, a theoretical study of the influence of the changing micro-structure on the mass transport is needed to study the feasibility of this new technology. This could be done by such a micro-structural model which is capable of determining effective transport parameter that can be used for multi-physics models in cell simulations.

The diffusion through the micro-structure of the porous support can be determined by use of a numerical method, e.g. computational fluid dynamics (CFD), Lattice Boltzmann method (LBM) or the finite element method. However, it would be unfeasible with current computational power to represent a full SOFC stack for that sake by this approach. Thus, in a multi-scale modelling approach the accurate micro-structural models can be utilised to determine the response of the smaller scale model. The results can be represented through homogenised material parameters in homogenised continuum models [33]. Hereby an accurate description of the flow is ensured together with a reduction of computational cells and required computer time by a factor of 10^5 or more. By this approach more fundamental knowledge about the material parameters and the occurring physical phenomena are obtained.

In homogenisation a boundary value problem is posed and solved to obtain the homogenised material parameters [34–36]. The boundary conditions for the flow problem can either be the flux, concentration or a periodic boundary condition. It has become customary to compute the effective diffusion coefficient for diffusion through the thickness of the cell by applying symmetry condition (concentration gradient perpendicular to the boundary equals zero) for the lateral boundary (parallel to the main diffusion path) [15–19]. This effectively introduces dead-end pores, or in other words blocks tortuous paths involving diffusion in and out of the domain in the vicinity of the lateral boundary. The only work-around so far is to perform the simulation on a sufficiently large volume that suppresses any impact of the lateral boundaries, but requires a much larger volume to be reconstructed and more computing power and time to perform the simulation. In Ref. [16] it was shown that with increasing size of the base area the values of interest converge because the error due to the transport via the lateral boundaries decreases. Nevertheless, no comparison between periodic and zero gradient boundary conditions and their influence was made. So far the effect of different boundary conditions for the top and bottom boundaries is analysed by Ref. [20], but not for the lateral faces.

In this work homogenised parameters of a metal-support of a metallic supported SOFC are determined. This will be a first step toward a degradation model in order to understand the impact of corrosion on the long term performance of metallic supported SOFCs by obtaining the effective diffusion coefficient of the porous structure, which is an important input parameter for the simulation of a multi-scale SOFC model. The parameters are determined with a more accurate method for homogenisation, where the domains in the vicinity of the lateral boundaries are not blocked for flow, i.e. by use of periodic boundary conditions. Furthermore, the influence of the inaccurate application of boundary conditions on the effective transport properties will be investigated. Also the concepts of tortuosity τ and the tortuosity-factor τ^2 are discussed in detail for further correct use of the results determined in this work. The inhomogeneous nature of the micro-structure will be addressed and analysed by determining the porosity distribution. In addition to that, the transport parameters of the different dense layers are evaluated, which is relevant in inhomogeneous micro-structures. Finally, the size of a stochastic equivalent representative volume element (SERVE) [15,16,20] and its limitations in inhomogeneous micro-structures are discussed.

2. Reconstruction of the micro-structure

In this paper the porous support of a metal-supported SOFC produced at Technical University of Denmark is analysed. The support is made by tape casting of a slurry with metallic powder and by subsequent sintering in a hydrogen furnace. For processing details please refer to Ref. [37]. A comprehensive description of the entire cell can be found in Ref. [2], a detailed characterisation via electro-chemical impedance spectroscopy is reported in Ref. [38]. The sample is a sintered half-cell (porous metal-support, anode functional layer and electrolyte) and has not been exposed to any operation, thus no corrosion has taken place in it.

The reconstructed micro-structure of this metal-support is obtained by X-ray CT scanning and by use of an in-house algorithm [39] for generating a computational mesh. The imaging was done with a SkyScan 1172 X-ray micro-CT system, equipped with a 100 keV X-ray source and an 11 megapixel (4000 × 2670 pixel) X-ray detector. A volume of 1.1 mm × 2.2 mm × 0.37 mm was scanned with a frame averaging of two and a rotation step of 0.36, so that the entire thickness of the actual metal-support is covered. The X-ray CT scan provides a stack of images a single of these can be seen in Fig. 1 together with its segmented counterpart, where the material is white and the pores are black. The gas-channel will be on top of this sintered half cell. The lower part comprises the anode functional layer (AFL) and the gas tight electrolyte. The evaluation

in this work is limited to the porous metal-support. The in-house algorithm regenerates the micro-structure into a computational mesh, by analysing the 2-D grey-scale images obtained with X-ray CT-scans. These 2-D images are combined to a 3-D grey-scale image. The images are digitised and reconstructed using statistical-functions [26–28]. With this information the algorithm determines positions, where pores or metal are prevailing. Thus, a 3-D voxel mesh can be reconstructed, which represents the real micro-structure. A 3-D plot of the micro-structure obtained by this method is shown in Fig. 2. The obtained result is written in a format that can be read by many CFD software packages.

3. Theory

In this section the background for determining the homogenised parameters, i.e. porosity, surface area, tortuosity and effective diffusion coefficients will be presented.

3.1. Porosity

Once the micro-structure is reconstructed, the determination of an averaged porosity ε is straightforward:

$$\varepsilon = \frac{n_{vo} V_{vo}}{V_e}, \tag{1}$$

where V_{vo} is the volume of one pore voxel, n_{vo} the number of pore voxels, and V_e the entire volume of the considered domain. The value of the porosity can easily be determined by measurements [33] and does not necessarily need the effort of micro-structural reconstruction. However, it is possible to retrieve the spatial distribution of the porosity, which is an important information and is described in Section 4.2 and shown in Fig. 3.

3.2. Surface area

The reconstruction algorithm also determines the specific surface area (surface area normalised by the phase volume) of the regenerated mesh. The results would be misleading because the voxel mesh overestimates the surface area. A rescaling factor r of $\Pi/6$ is proposed [20], but this only relates the surface of sphere to its circumscribed cube. The reconstructed mesh approximates the surface, as well as the volume. Therefore, a rescale factor for the specific surface area has to be found. In the above case the specific surface area of the sphere and the circumscribed cube would be the same. Basically, the rescale factor depends on the voxel resolution and the algorithm's capability of recreating the structure with
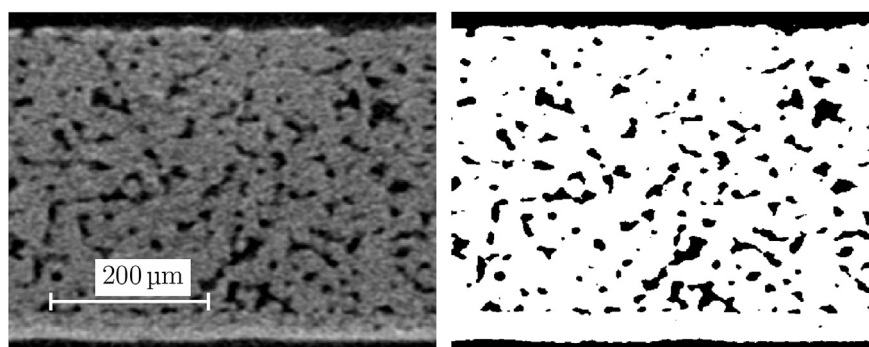
Fig. 1. Left-hand side shows a single 2-D image representing a slice through the obtained 3-D micro-structure with X-ray CT-scans. The digitalised binary image is shown on the right hand side (white → material, black → pores). The gas-channel would be on top. The lower parts show the anode functional layer (AFL) and the dense electrolyte. The evaluation is confined to the porous metal-support.
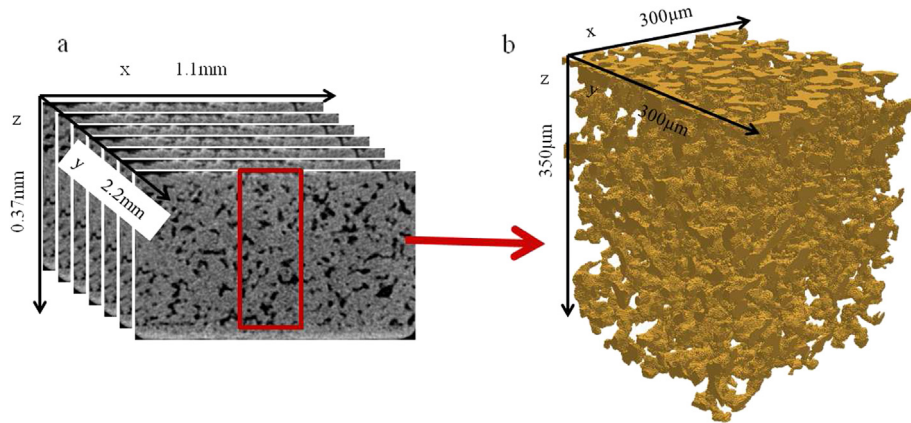
Fig. 2. a) Image stack obtained with X-ray CT-scans of a sintered half cell. On the bottom the anode functional layer and the gas tight electrolyte can be seen. For the reconstruction only the porous metal-support is evaluated. b) Reconstructed computational geometry of the pores with a voxel length of 1.0×10^{-6} m.

voxel. The relation between the specific area of the sphere and its voxelised cubic counterpart is:

$$\frac{6}{d} = r \frac{6 n_{vo,A}}{s n_{vo}} \tag{2}$$

with

$$r = \frac{s}{d} \frac{n_{vo}}{n_{vo,A}}. \tag{3}$$

The diameter of the sphere is d, the voxel length is s and $n_{vo,A}$ stands for the number of surface voxel at each side of the voxelised sphere. The fraction $n_{vo}/n_{vo,A}$ accounts for the algorithm's capability to reconstruct the sphere. The mean uncorrected specific surface area for the metal-support is 0.117 μm^{-1}.
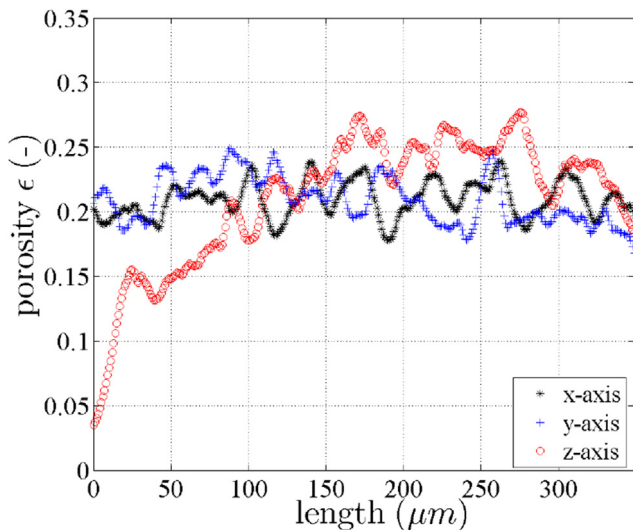
Fig. 3. Porosity distribution along the three coordinate axes for the windowing geometry with a base area of 350 μm $\times$ 350 μm. The z-direction is the diffusion path from the gas-channel to the anode functional layer. While the directions parallel to the gas-channel show a homogeneous porosity distribution, the diffusion path orthogonal to the gas channel has a much lower porosity in the first 50 to 100 μm compared to the rest of the electrode. The gas-channel interface is located at 0 μm and the interface to the anode functional layer at 350 μm.

3.3. Tortuosity

The tortuosity τ is more difficult to determine. Many different definitions of the tortuosity exist in literature [40]. A geometrical definition of the tortuosity in 2-D is the ratio between the length of the actual or effective path L_{eff} and the straight and shortest possible distance L between two points:

$$\tau = \frac{L_{eff}}{L}. \tag{4}$$

There are attempts to determine the tortuosity experimentally through saturation current density measurement [41], or mercury intrusion porosimetry (MIP) [42], although the parameter cannot be measured directly [40]. Computation of it, is therefore an excellent alternative. The geometrical tortuosity can be calculated by the fast marching method [43] or the centre of mass calculations [17]. Another possibility is to simulate a transport through the related phase (here pores) and analyse the impact of the other phases (here metal backbone of the support) on the transport properties. In Ref. [15] a tortuosity was obtained by solving the Laplace equation for the electrical potential, which provides the ratio of effective conductivity to bulk conductivity of the related phase. In this paper the tortuosity is determined by simulating the diffusive flux through the pores and calculating an effective diffusion coefficient. In this case the tortuosity equals a kinematic property, comparable to the relative average length of the flow path of a fluid particle from one side of a porous structure to the other. Its original introduction in SOFC models was also intended as a kinematic property [13]. The advantage is that it is directly related to the effective transport properties of the layer and thus can be used for performance simulations.

3.4. Effective diffusion coefficient

Fick's law is the simplest form to describe binary diffusion [12]. In 1-D the molar flux N_a can be calculated by:

$$N_a = -c_{gas} D_{ab} \frac{\Delta x_a}{L}, \tag{5}$$

where D_{ab} is the binary diffusion coefficient, for example $a = H_2$ and $b = H_2O$, c_{gas} is the gas concentration, Δx_a is the difference in the mole fraction, and L is the length between the gas-channel and the anode functional layer, which is in this case equivalent to the thickness of the metal-support. Consequently, the diffusive fluxes

depend on their diffusion coefficients and the prevailing driving forces (here: molar concentration). Several models are available to describe the binary diffusion coefficient D_{ab}, see e.g. Ref. [44]. In the presence of porous media, diffusion is impeded by the porosity and the tortuosity. This is taken into account by introducing an effective binary diffusion coefficient D_{ab}^{eff} in porous media [44–48]:

$$N_a^{\text{porous}} = -c_{\text{gas}} D_{ab}^{\text{eff}} \frac{\Delta x_a}{L}, \qquad (6)$$

where N_a^{porous} is the superficial axial diffusion.

According to Refs. [33,49] also the underlying driving force is influenced by the tortuosity. The definition of the average diffusional flux through the pores is:

$$N_{a,\text{p}} = -c_{\text{gas}} D_{ab} \frac{\Delta x_a}{L_{\text{eff}}}, \qquad (7)$$

where L_{eff} is the actual pore length. The superficial axial diffusion can be related to the interstitial axial diffusion $N_{a,\text{i}}$ by

$$N_a^{\text{porous}} = N_{a,\text{i}}\, \varepsilon. \qquad (8)$$

The residence time t of species a in the porous medium can be expressed either by the interstitial axial diffusion:

$$t = \frac{L\, c_{\text{gas}}}{N_{a,\text{i}}}, \qquad (9)$$

or the diffusional flux through the pores:

$$t = \frac{L_{\text{eff}}\, c_{\text{gas}}}{N_{a,\text{p}}}. \qquad (10)$$

Combining equations (8)–(10) results in:

$$N_{a,\text{p}} = \frac{N_a^{\text{porous}}}{\varepsilon} \frac{L_{\text{eff}}}{L}. \qquad (11)$$

Inserting equation (11) into (6) and using the definition of the tortuosity from equation (4) yields after rearranging:

$$N_a^{\text{porous}} = -c_{\text{gas}} \frac{\varepsilon}{\tau^2} D_{ab} \frac{\Delta x_a}{L}. \qquad (12)$$

Comparing equations (12) and (6) and defining the scaling factor f as $D_{ab}^{\text{eff}} = f D_{ab}$ it should read:

$$f = \frac{\varepsilon}{\tau^2}, \qquad (13)$$

as was correctly mentioned by Refs. [18,50]. The effective diffusion coefficient is an important parameter, used to describe the transport in homogenised electrode models [51]. It is often employed as a fitting parameter in macro-scale simulations [13,52–54], why the misinterpreted use of the scaling factor $f = \varepsilon/\tau$ instead of $f = \varepsilon/\tau^2$ is not crucial. However, in micro-structural modelling the actual molar flux in the reconstructed, tortuous geometry is computed and compared with equation (6), which would be the macroscopic approach to calculate the molar flux in a homogenised geometry. Thus it is important to use the correct formulation of the scaling factor given in equation (13).

The procedure to calculate the scaling factor is presented in Section 4.1. When using the actual micro-structure this factor also includes a correction for pockets and dead-end pores. In addition to this, Ref. [55] explained that not only the longer path length has to be taken into account, but also the existence of small orifices, which impedes diffusion. To sum up, the calculated scaling factor

allows the estimation of the tortuosity of the micro-structure, but this value does not necessarily equal the geometrical definition of the tortuosity, given in equation (4), for the reasons mentioned above.

4. Methodology

4.1. Calculation of the effective diffusion coefficient

The solution of the diffusion transport equation provides the distribution of the molar fraction x. This approach can also be applied for electrons or ions, as their transport is described by the same formulation. Considering steady-state conditions and no external body forces, it can be written for the mass diffusion as follows:

$$\nabla(-D_{ab}\nabla x_a) = 0. \qquad (14)$$

Dirichlet boundary conditions $x = x_t$, $x = x_b$ are often applied on the top and bottom surfaces [15,16,18,19,56], while the gas–solid interface is a Neumann boundary (zero-flux). The influence of the boundary conditions on the top and bottom surfaces was investigated and Dirichlet and Neumann boundary conditions were compared [20]. It was shown, that different results were obtained and an intermediate boundary condition (fixed concentration on top and fixed flux on bottom) was proposed as best practice. In all these works the remaining boundaries of the computational domain are typically set to a zero-flux Neumann condition $\nabla x = 0$, as this is often applied to represent symmetry. It was discussed in the Introduction, that this models reality only in an approximate way, as this effectively introduces a lot of dead-end pores, or in other words blocks tortuous paths involving diffusion in and out of the domain in the vicinity of the lateral boundary.
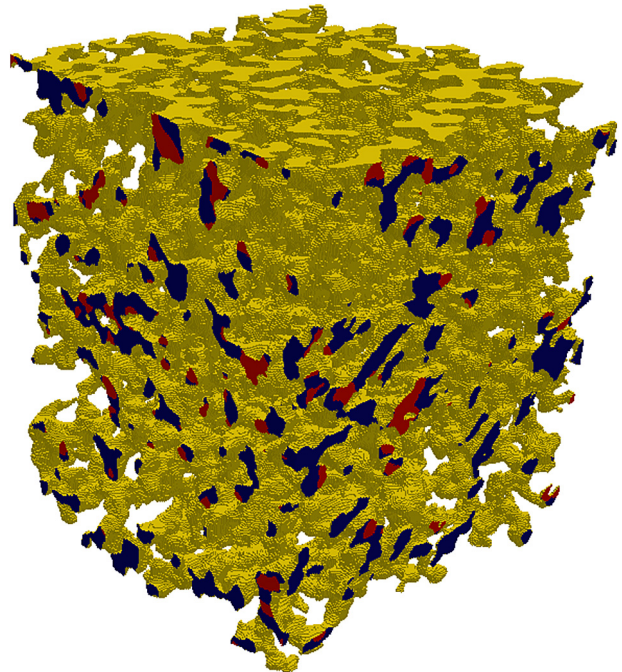
Fig. 4. Pore volume of the computational geometry with lateral boundaries shown in dark blue → zero gradient and red → periodic boundary. Periodic boundary conditions are applied wherever possible. The size of the geometry is 300 μm × 300 μm × 350 μm and the diffusion path is from top to bottom. (For interpretation of the references to colour in this figure legend, the reader is referred to the web version of this article.)

A more realistic approach is to use so-called periodic boundaries for this lateral boundary to the highest feasible extent, as is done in many different fields [36,57–59]. This means that the mass, which leaves the computational geometry at one side, enters at the opposite. This would also be the case in reality, where the pores will leave and enter the examined geometry. In Fig. 4 the computational geometry is shown. The diffusion path is from top to bottom and the lateral boundary are shown. For boundary regions, where a porous path is continued on the opposite side of the considered domain, a periodic boundary condition is set. These boundary regions are coloured red. The blue coloured boundary regions signifies porous paths with no counterpart on the opposite side, why they are effectively blocked in this simulation. These are coloured blue. This new approach will lead to a better prediction of the scaling factor because the zero-flux Neumann condition can lead to an overestimation of the scaling factor, since many of the prevailing pores are then supposed to be dead-end pores.

The diffusion equation (14) is numerically solved by integrating over the computational cell and applying the Gauss-theorem. The surface integral is then discretized using the finite volume method (FVM) based on the open-source CFD toolkit *OpenFOAM* [60]:

$$\int_{V_p} \nabla(D_{ab}\nabla x_a)dV = \sum_f \boldsymbol{S}_f(D_{ab}\nabla x_a) = 0,$$ (15)

where V_p is the control volume of one computational cell, the subscript f denotes a face of this control volume, and $\boldsymbol{S}_f$ is the surface normal vector of the face. Once the distribution of x is calculated the averaged local flux ϕ across the boundary surface can be calculated:

$$\int_S \phi dS = \int_S -D_{ab}\nabla x_a \boldsymbol{n} dS,$$ (16)

and hence the effective diffusion coefficient can be determined:

$$D_{ab}^{\mathrm{eff}} = \frac{\int_S -D_{ab}\nabla x_a \boldsymbol{n} dS}{\left(\frac{\triangle x_a}{L}\right)A}.$$ (17)

The denominator in equation (17) represents the molar flux calculated with equation (6) in the homogenised geometry across the area A. The difference in the mole fraction $\triangle x_a$ is calculated as the difference of the weighted averaged mole fraction at the top and bottom surfaces. Here the same approach as Ref. [20] proposed, is pursued and different boundary conditions (Dirichlet, Neumann) are applied to the top and bottom boundaries. A similar tendency is observed:

1 Two fixed mole fractions on the top and bottom boundaries (Dirichlet) result in the lowest tortuosity value.
2 Two fixed fluxes on the top and bottom boundaries (Neumann) yield the highest tortuosity value.
3 The tortuosity value obtained with a fixed mole fraction on the top and a defined flux on the bottom boundary lies between the above approaches.

In this paper the last approach is used as this resembles the nature of an SOFC most adequately, see also Ref. [20].

With the effective diffusion coefficient and the definition of the scaling factor f in equation (13) the tortuosity of the micro-structure can be determined:

$$\tau = \sqrt{\varepsilon \frac{D_{ab}}{D_{ab}^{\mathrm{eff}}}}.$$ (18)

4.2. Calculation of a 3-D porosity distribution

In Section 3.1 the calculation of an averaged porosity is described, which can be used in cell and stack simulation. In order to justify the efforts of a reconstruction a *MATLAB* algorithm was programmed, which analyses the micro-structure and computes i.e. the porosity distribution, the mean pore diameter, the pore number, the pore area size and orientation along all directions. This gives a realistic picture of the inhomogeneity of the micro-structure leading to anisotropic transport properties. The basic procedure of the algorithm is as follows:

1 The coordinates of each computational cell serve as an input parameter for the algorithm.
2 One coordinate axis can be chosen. The sample is subdivided into slices orthogonal to this axis (see left hand side Fig. 5).
3 Every slice is processed using the standard *MATLAB Image Processing Toolbox*, which distinguishes spatially separated pore cross sections (see right hand side Fig. 5).
4 These cross-sections are analysed, and the results can be plotted along the previous defined axis.

Exemplary results of the porosity distribution for different sample positions are plotted in Fig. 3. The distribution of the mean pore diameter is shown in Fig. 6, and the pore number is presented in Fig. 10.

4.3. Representative reconstructed geometries

The procedure for calculating averaged parameters out of a reconstructed micro-structure is limited by computational capacity. The larger the investigated volume, the more computational cells are needed to mesh the domain, the longer are the calculation times, but it is more representative for the entire cell. When dealing with an inhomogeneous material the results of the averaging processes depend on the position, where the sample is taken and on the sample size [33]. In order to decide whether or not the sample size is large enough a stochastic equivalent representative volume element (SERVE) is determined [15,16,20], by the so-called windowing technique. In windowing the volume of the investigated geometry is increased until e.g. the change of the desired homogenised parameter (e.g. porosity) drops below a desired threshold. However, the analysis is limited to one location of this sample, which was taken out of one place of a larger cell. This approach is applicable, if it can be assumed that the micro-structure is more or less homogeneous. In order to get a more representative result, it is important to use reconstructed geometries from different positions of the sample, as done in this work. The importance of this can be understood when looking at Fig. 3. The inhomogeneous nature of the metal-support can be seen in the huge difference of the porosity in the first 100 μm compared to the remaining part. Determining a SERVE and starting from the wrong position may lead to wrong results. Therefore, the entire height of 350 μm is considered in this paper and the base area of the reconstructed geometries is increased, while the centre point stays the same for each geometry.

5. Results

The transport parameters are evaluated using a 3-D reconstruction of a metal-support with subsequent numerical
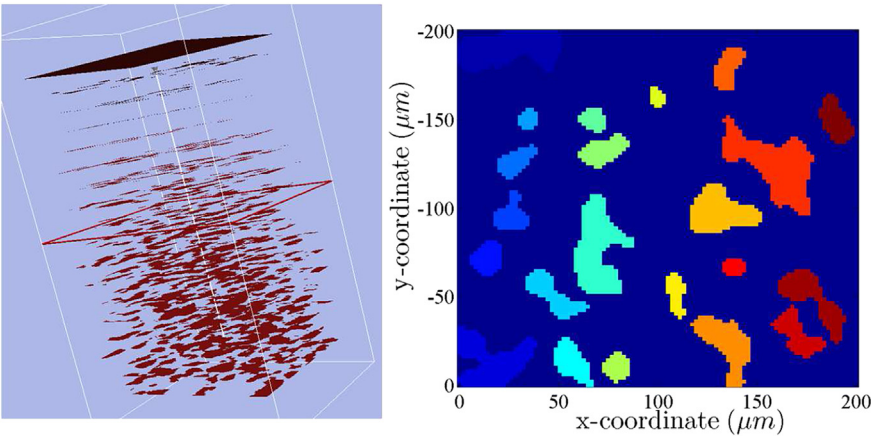
Fig. 5. Computational geometry is cut into slices (left hand side). These slices are analysed with *MATLAB* and their size, orientation, shape, area and diameter is determined. Right hand side shows an evaluated sample slice, where connected pores are highlighted in different colours. (For interpretation of the references to colour in this figure legend, the reader is referred to the web version of this article.)
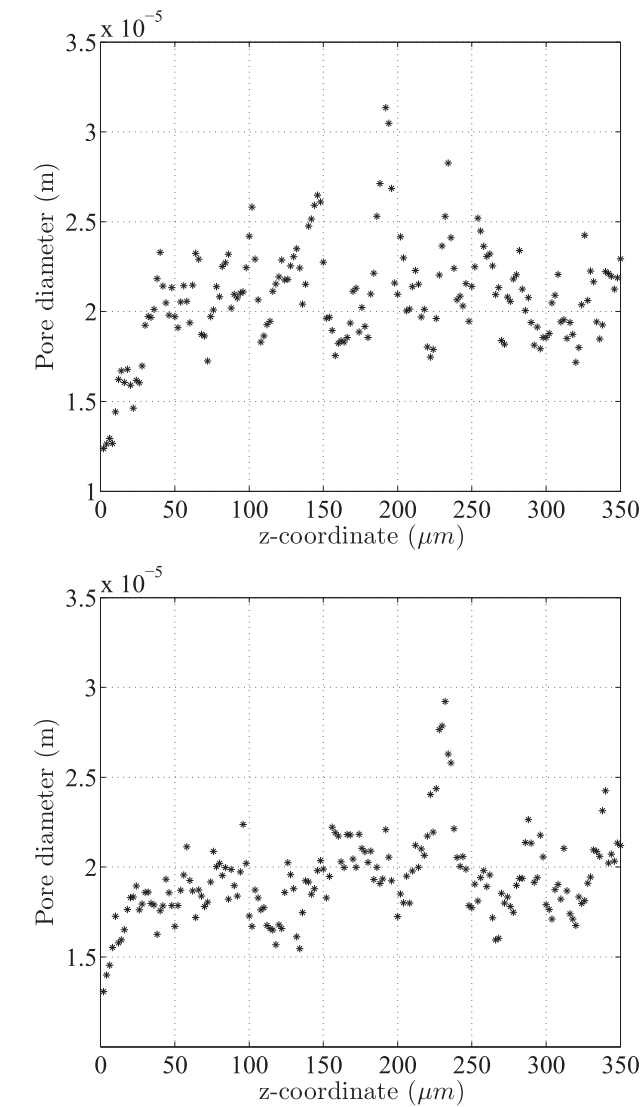
Fig. 6. Mean pore diameter distribution along the diffusion path for two different positions in the sample. The gas-channel interface will be at 0 μm and the interface to the anode functional layer at 350 μm.
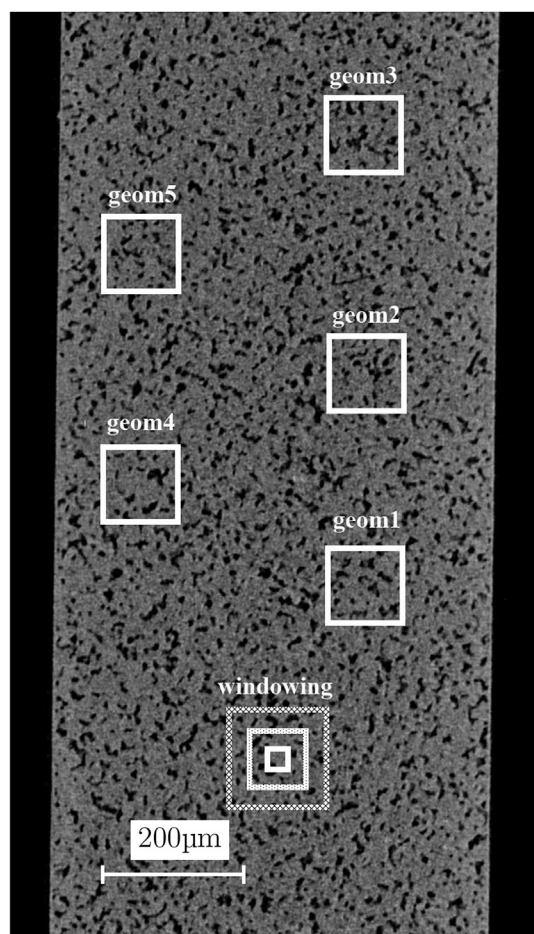
computation. The obtained homogenised parameters for the porous metal-support are shown in Table 1 and the different sample positions are depicted in Fig. 7. The homogenised mean porosity for five different sample positions is 0.200 and the mean equivalent diameter is 18.1 μm. The value for the homogenised computed tortuosity is 4.3 calculated with equation (18). It was discussed in Section 3.4 and stressed again here, that the calculated tortuosity from the micro-structural computation also includes effects like dead-end pores, orifices and pockets and does not necessarily equal the geometrical definition of the tortuosity given in equation (4). It has to be noted, that these values correspond to an uncorroded micro-structure and may decrease during operation and expected corrosion of the metal-support. This issue is subject to further development of a corrosion model.

The computed scaling factors are compared to measurement results already published for a similar cell design [2]. There are only minor differences in porosity and pore-size distribution of the metal-support between the simulated and the tested cell. Based on electro-chemical impedance spectroscopy and a subsequent impedance data analysis by the distribution of relaxation times, the individual loss mechanisms could be identified. The area specific resistance, which is related to gas diffusion processes in the substrate, is extracted and fitted with a model proposed by Ref. [14]. The fitting result for the scaling factor f, which describes the diffusion process in the metal-support, is 1.32×10^{-2}. The comparison of the results is summarised in Table 2, where the statistical

Table 1

Comparison of micro-structural parameters, obtained from 3-D reconstruction/modelling, for five different computational geometries, with a base area size of 200 μm × 200 μm. The subscript hom refers to the overall homogenised parameter calculated with a height of 350 μm. The dense-parameters are evaluated only in the first 100 μm, where a significant lower porosity was found (see Fig. 3). Parameters with the subscript porous are computed in the remaining region (from 100 to 350 μm). The principal positions of the geometries are shown in Fig. 7, and Fig. 8 depicts the positions of the different layers.

	Mean value	Standard deviation
ε_{hom}	0.200	0.009
Scaling factor f_{hom}	1.19×10^{-2}	4.8×10^{-3}
τ_{hom}	4.3	0.81
Pore diameter (μm)	18.1	0.51
ε_{dense}	0.147	0.006
Scaling factor f_{dense}	0.84×10^{-2}	4.03×10^{-3}
ε_{porous}	0.219	0.013
Scaling factor f_{porous}	1.94×10^{-2}	5.7×10^{-3}

Fig. 7. Position of the arbitrarily chosen samples. It is ensured that the sample positions don't overlap and a certain distance is kept to the edges.

Another interesting finding, which can be seen in Table 2 is that the difference between the zero gradient and periodic boundary conditions is about 46.9% and that the more accurate periodic approach shows a better agreement with the measurement data. This supports and proves the assumption that the incorrect application of zero gradient boundary conditions at the lateral walls introduces additional dead-end pores which reduce the entire mass transport through the micro-structure and leads to a smaller the scaling factor.

One explanation for the low scaling factor is, that this could be due to the dense first 100 μm from the gas-channel to the anode functional layer, where also the number of pores is much lower compared to the rest of the metal-support, as shown in Fig. 10. Therefore, a more thorough analysis of the metal-support micro-structure is conducted. In addition to the homogenised transport parameters for the whole micro-structure, the denser first 100 μm, as well as, the remaining more porous 250 μm are assessed separately, see Fig. 8 for a sketch of the layers. A comparison is shown in Table 1, again with the statistical values of five different computational geometries. Going from the gas-channel to the anode functional layer the first 100 μm of the metal-support have an averaged porosity of 0.147 and a scaling factor of 0.84×10^{-2}. The region from 100 to 350 μm has an averaged porosity of 0.219 and a scaling factor of 1.94×10^{-2}. The difference in the scaling factors is about 130%, which allows to draw the conclusion, that the results of a cell model, calculated with two different layers will be more accurate than those using an overall homogenised approach.

Another problem addressed, is the question of how to find a stochastic equivalent representative volume element (SERVE). The state-of-the-art approach is explained and its drawbacks can be assessed by this inhomogeneous micro-structure. As shown in Fig. 3 the porosity in the first 100 μm, from the gas-channel to the anode functional layer, is much lower compared to the rest of the

values of five different, reconstructed geometries are presented. The positions of these geometries are shown in Fig. 7. Comparing the computed and measured/fitted scaling factor it can be seen that the values are in the same order of magnitude and that the suggested approach with periodic boundary conditions yields a value of 1.19×10^{-2}, which deviates only by 11% from the measurements. Given the differences of the two studied cells this is an expected deviation. Furthermore, the scaling factor in Table 2 of the metal-support is much smaller, by a factor of 20, compared to values, which are commonly employed in macro-scale simulations and are in the range of $10-25 \times 10^{-2}$ [47,48,50,54,61,62]. However, it has to be mentioned, that in these works the scaling factor was used as a fitting parameter for the applied simulation models, and was not determined either by measurement/fitting or 3-D reconstruction/modelling.
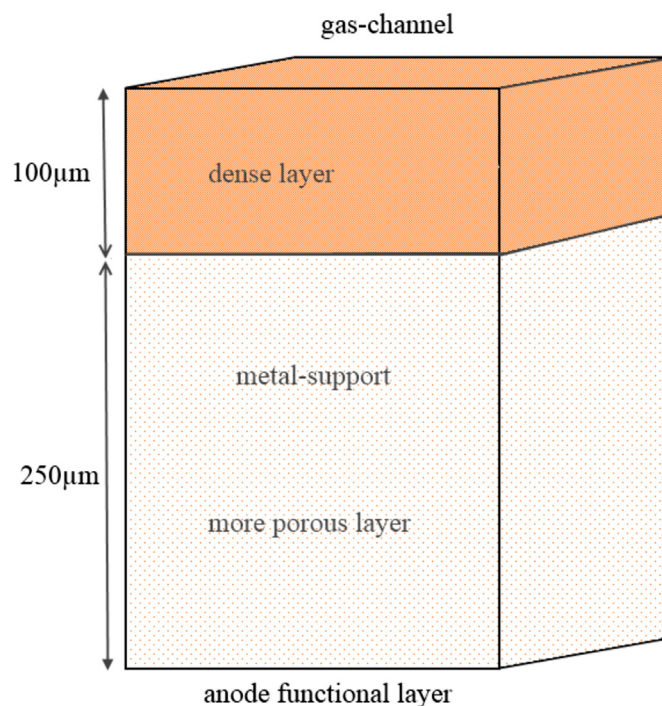
Table 2
Comparison of the mean values and standard deviations of scaling factors for different boundary conditions calculated on the same computational geometries to the value obtained from impedance measurements which is 1.32×10^{-2}. The base area is in all cases 200 μm × 200 μm and the height is 350 μm.

Boundary condition (BC)	Scaling factor ($\times 10^{-2}$)		Diff (%)
	Mean value	Standard deviation	
Measurement	1.32		
Zero gradient	0.81	0.41	63.0
Periodic	1.19	0.477	10.9

Fig. 8. Principal depiction of the metal-support with the 100 μm thick dense upper layer (referred to as dense) and the more porous 250 μm of the remaining metal-support (referred to as porous). Homogenised parameters (referred to as hom) are calculated for the entire height of 350 μm.
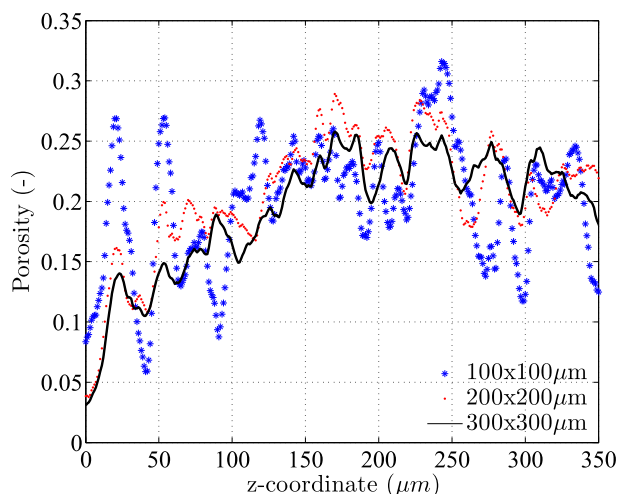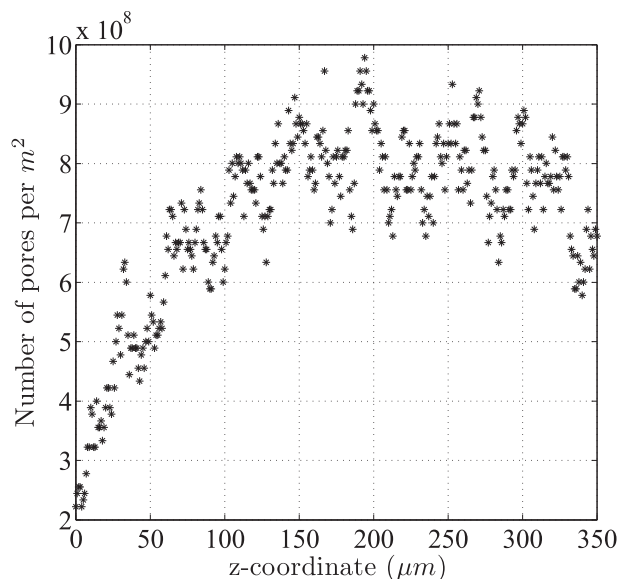
Table 3
Porosity values, scaling factor and number of computational cells for a geometry height of 350 μm and increasing base area. The geometry with a base area of 50 μm × 50 μm has not got a continuous pore from the gas-channel to the anode functional layer interface.

Area ε_{dense}	Porosity (−)	Scaling factor (−) (×10^{-2})	Number of computational cells
50 × 50	0.193	−	0.2×10^6
100 × 100	0.196	2.11	0.7×10^6
150 × 150	0.206	1.90	1.6×10^6
200 × 200	0.206	1.99	2.9×10^6
250 × 250	0.192	1.69	4.2×10^6
300 × 300	0.193	1.35	6.1×10^6
350 × 350	0.209	1.73	9.0×10^6

micro-structure. This may be due to the sintering process, and is subject to further investigation. When a SERVE is determined the volume of the reconstructed geometry is increased till the parameters remain constant within a certain tolerance. Nevertheless, increasing the SERVE and starting from the anode functional layer, a SERVE might be found in the metal-support micro-structure before the dense region near the gas-channel is reached. This means that without the knowledge about the (in-)homogeneity of the micro-structure the starting point of the SERVE investigation may lead to a wrong assessment of the micro-structure. Therefore, it was attempted to use the entire height of the metal-support for the determination of a SERVE and the assessment of transport parameters in this paper. Starting with a base area of 50 μm × 50 μm, the area is gradually increased and the micro-structural parameters determined. The porosity value and the scaling factor along with the number of computational cells are listed in Table 3. Although the volume of the reconstructed geometry is increased, the porosity and the tortuosity vary and no clear convergence of the parameters can be found. In Fig. 9 the porosity distribution is plotted along the diffusion path for increased base areas. Here again the deviation of the porosity decreases, but the volume is still not sufficiently large, although it exceeds the size of SERVEs reported in literature by orders of magnitude [16—18,20]. Furthermore, the rather high deviations of the scaling factors in Table 2 indicate that the metal-support is inhomogeneous and the results of the computational evaluation of the micro-structure highly depends on the chosen

Fig. 10. Number of pores per m² along the diffusion path. In the first 100 μm there are less pores compared to the rest of the metal-support. The gas-channel interface will be at 0 μm and the interface to the anode functional layer at 350 μm. The base area is 200 μm × 200 μm.

location. This confirms the approach of this paper to use several different sample locations and average the retrieved micro-structural parameters, as well as, to distinguish different layers and to determine the individual transport parameters separately.

6. Conclusion

In this paper the computational framework for the investigation of homogenised parameters of a porous metal-support for metal-supported SOFC has been presented. A more realistic set of boundary conditions for homogenisation was introduced. It was shown that for the considered micro-structure a significant error is committed by applying the commonly used zero flux boundary condition on the lateral boundaries, and that the usage of the more accurate periodic boundary condition to the highest feasible extent is recommended. The values of the homogenised scaling factor for the effective diffusion coefficient for the metallic support was determined to be approximately 1.2×10^{-2}. The results are compared to impedance spectroscopy measurement and showed good agreement. In order to assess the inhomogeneity of the micro-structure the porosity distribution, as well as, the transport parameters of two identified, different dense layers of the metal-support were evaluated. The presented model is a first step toward a study of the influence of corrosion on the effective transport parameters.

Fig. 9. Porosity distribution for reconstructed geometries with the same centre point and increasing base areas. Although the base area is increased the porosity distribution still changes and no SERVE is obtained. The gas-channel interface will be at 0 μm and the interface to the anode functional layer at 350 μm.

Nomenclature

ε	porosity $(-)$
τ	tortuosity $(-)$
τ^2	tortuosity factor $(-)$
ϕ	flux e.g. molar flux $(kmol\ m^{-2}\ s^{-1})$
N_a	molar flux of species a $(kmol\ m^{-2}\ s^{-1})$
N_a^{porous}	molar flux of species a in porous medium $(kmol\ m^{-2}\ s^{-1})$
$N_{a,i}$	axial interstitial molar flux of species a in porous medium $(kmol\ m^{-2}\ s^{-1})$
$N_{a,p}$	average diffusional molar flux of species a through the pores of a porous medium $(kmol\ m^{-2}\ s^{-1})$
S_f	surface normal vector of face (m^2)
A	base area of the homogenised geometry (m^2)
c_{gas}	concentration $(kmol\ m^{-3})$
d	diameter of a sphere (m)
D_{ab}	binary diffusion coefficient $(m^2\ s^{-1})$
D_{ab}^{eff}	effective binary diffusion coefficient $(m^2\ s^{-1})$
f	scaling factor $(-)$
L	length (m)
L_{eff}	effective length (m)
$n_{vo,A}$	number of voxel at the surface $(-)$
n_{vo}	number of voxel $(-)$
r	rescaling factor for specific surface area $(-)$
s	length of one voxel (m)
t	residence time (s)
V_e	volume of computational domain (m^3)
V_p	control volume of one computational cell (m^3)
V_{vo}	volume of one voxel (m^3)
x_a	mole fraction of species a $(-)$

References

[1] P. Blennow, J. Hjelm, T. Klemenso, A.H. Persson, S. Ramousse, M. Mogensen, Fuel Cells 11 (2011) 661—668.

[2] P. Blennow, J. Hjelm, T. Klemenso, S. Ramousse, A. Kromp, A. Leonide, A. Weber, J. Power Sources 196 (2011) 7117—7125, 9th European SOFC Forum, Lucerne, Switzerland, 2010.

[3] M.C. Tucker, G.Y. Lau, C.P. Jacobson, L.C. DeJonghe, S.J. Visco, J. Power Sources 171 (2007) 477—482.

[4] M.C. Tucker, G.Y. Lau, C.P. Jacobson, L.C. DeJonghe, S.J. Visco, J. Power Sources 175 (2008) 447—451.

[5] M.C. Tucker, J. Power Sources 195 (2010) 4570—4582.

[6] Y.B. Matus, L.C.D. Jonghe, C.P. Jacobson, S.J. Visco, Solid State Ionics 176 (2005) 443—449.

[7] T. Franco, M. Haydn, R. Mücke, A. Weber, M. Rüttinger, O. Büchler, S. Uhlenbruck, N.H. Menzler, A. Venskutonis, L.S. Sigl, ECS Trans. 35 (2011) 343—349.

[8] T. Franco, R. Mücke, A. Weber, M. Haydn, M. Rüttinger, N.H. Menzler, A. Venskutonis, L.S. Sigl, H.P. Buchkremer, in: F. Lefebbvre-Joud, Lefe (Eds.), Proceedings of the 10th European Solid Oxide Fuel Cell Forum, Lucerne, Switzerland, A0906 49—A0906 61.

[9] T. Franco, M. Haydn, A. Weber, W. Schafbauer, L. Blum, U. Packbier, D. Roehrens, N.H. Menzler, J. Rechberger, A. Venskutonis, L.S. Sigl, H.P. Buchkremer, ECS Trans. 57 (2013) 471—480.

[10] J. Nielsen, T. Klemenso, P. Blennow, J. Power Sources 219 (2012) 305—316.

[11] B. Haberman, J. Young, Int. J. Heat Mass Transf. 47 (2004) 3617—3629.

[12] R. Bove, S. Ubertini, Modeling Solid Oxide Fuel Cells: Methods, Procedures and Techniques, Springer, 2008.

[13] M. Andersson, J. Yuan, B. Sunden, Appl. Energy 87 (2010) 1461—1476.

[14] A. Leonide, V. Sonn, A. Weber, E. Ivers-Tiffée, J. Electrochem. Soc. 155 (2008) B36—B41.

[15] J. Joos, T. Carraro, A. Weber, E. Ivers-Tiffe, J. Power Sources 196 (2011) 7302—7307.

[16] J. Joos, M. Ender, T. Carraro, A. Weber, E. Ivers-Tiffe, Electrochim. Acta 82 (2012) 268—276.

[17] D. Gostovic, J.R. Smith, D.P. Kundinger, K.S. Jones, E.D. Wachsman, Electrochem. Solid-State Lett. 10 (2007) B214—B217.

[18] N. Vivet, S. Chupin, E. Estrade, T. Piquero, P. Pommier, D. Rochais, E. Bruneton, J. Power Sources 196 (2011) 7541—7549.

[19] N.S.K. Gunda, S.K. Mitra, J. Phys. Conf. Ser. 362 (2012).

[20] J. Laurencin, R. Quey, G. Delette, H. Suhonen, P. Cloetens, P. Bleuet, J. Power Sources 198 (2012) 182—189.

[21] J.R. Izzo, A.S. Joshi, K.N. Grew, W.K.S. Chiu, A. Tkachuk, S.H. Wang, W. Yun, J. Electrochem. Soc. 155 (2008) B504.

[22] P. Jorgensen, K. Hansen, R. Larsen, J. Bowen, J. Power Sources 195 (2010) 8168—8176.

[23] G.J. Nelson, W.M. Harris, J.J. Lombardo, J.R. Izzo Jr., W.K. Chiu, P. Tanasini, M. Cantoni, J. Van herle, C. Comninellis, J.C. Andrews, Y. Liu, P. Pianetta, Y.S. Chu, Electrochem. Commun. 13 (2011) 586—589.

[24] P. Shearing, J. Gelb, N. Brandon, J. Eur. Ceram. Soc. 30 (2010) 1809—1814.

[25] G. Borgefors, I. Nystrm, Pattern Recognit. Lett. 18 (1997) 465—471.

[26] J. Wang, Y. Tan, Pattern Recognit. 46 (2013) 230—242.

[27] W.-P. Choi, K.-M. Lam, W.-C. Siu, Pattern Recognit. 36 (2003) 721—729.

[28] C.L.Y. Yeong, S. Torquato, Phys. Rev. E 57 (1998) 495—506.

[29] S. Molin, B. Kusz, M. Gazda, P. Jasinski, J. Power Sources 181 (2008) 3137.

[30] S. Molin, M. Gazda, B. Kusz, P. Jasinski, J. Eur. Ceram. Soc. 29 (2009) 757762.

[31] S. Molin, M. Gazda, P. Jasinski, Solid State Ionics 181 (2010) 12141220.

[32] S. Molin, M. Gazda, P. Jasinski, J. Eur. Ceram. Soc. 31 (2011) 27072710.

[33] J. Bear, Dynamics of Fluids in Porous Media, 1988. Dover, New York.

[34] H. Yanagihara, W. Brandstätter, N. Ohashi, B. Gschaider, J. Leixnering, I. Stankovic, Top. Catal. 52 (2009) 1842—1846.

[35] E.M. Borla, G. Nicol, W. Brandstätter, M. Klug, New Concepts and Technologies for Integrated Diesel Exhaust Gas Aftertreatment Systems, SAE International, Warrendale, PA, 2011. SAE Technical Paper 2011-24-0184.

[36] A. Matine, N. Boyard, P. Cartraud, G. Legrain, Y. Jarny, Int. J. Heat Mass Transf. 62 (2013) 586—603.

[37] T. Klemenso, J. Nielsen, P. Blennow, S.H. Persson, T. Stegk, B.H. Christensen, S. Snderby, J. Power Sources 196 (2011) 9459—9466.

[38] A. Kromp, J. Nielsen, P. Blennow, T. Klemenso, A. Weber, Fuel Cells 13 (2013) 598604.

[39] J. Leixnering, B. Gschaider, W. Brandsttter, R. Bouwman, in: OpenFOAM International Conference, Old Windsor, UK.

[40] L. Shen, Z. Chen, Chem. Eng. Sci. 62 (2007) 3748—3755.

[41] C.-L. Tsai, V.H. Schmidt, J. Power Sources 196 (2011) 692—699.

[42] K.N. Grew, A.A. Peracchio, A.S. Joshi, J.R. Izzo Jr., W.K. Chiu, J. Power Sources 195 (2010) 7930—7942.

[43] P.S. Jorgensen, K.V. Hansen, R. Larsen, J.R. Bowen, J. Microsc. 244 (2011) 45—58. PMID: 21631501.

[44] V. Novaresio, M. Garcia-Camprubi, S. Izquierdo, P. Asinari, N. Fueyo, Comput. Phys. Commun. 183 (2012) 125—146.

[45] M. Garcia-Camprubi, A. Sanchez-Insa, N. Fueyo, Chem. Eng. Sci. 65 (2010) 1668—1677.

[46] P. Pisani, Int. J. Heat Mass Transf. 51 (2008) 650—660.

[47] W.G. Bessler, S. Gewies, M. Vogler, Electrochim. Acta 53 (2007) 1782—1800.

[48] T.X. Ho, P. Kosinski, A.C. Hoffmann, A. Vik, Chem. Eng. Sci. 63 (2008) 5356—5365.

[49] N. Epstein, Chem. Eng. Sci. 44 (1989) 777—779.

[50] S. Wang, W.M. Worek, W.J. Minkowycz, Int. J. Heat Mass Transf. 55 (2012) 3933—3945.

[51] S.B. Adler, J.A. Lane, B.C.H. Steele, J. Electrochem. Soc. 143 (1996) 3554—3564.

[52] F.N. Cayan, S.R. Pakalapati, F. Elizalde-Blancas, I. Celik, J. Power Sources 192 (2009) 467—474.

[53] Y. Vural, L. Ma, D.B. Ingham, M. Pourkashanian, J. Power Sources 195 (2010) 4893—4904.

[54] R. Suwanwarangkul, E. Croiset, M.W. Fowler, P.L. Douglas, E. Entchev, M.A. Douglas, J. Power Sources 122 (2003) 9—18.

[55] T.G. Sherwood, R.L. Pigford, C.R. Wilke, in: B. Clark, J. Maisel (Eds.), Mass Transfer, McGraw-Hill Inc., 1975, pp. 39—43.

[56] H. Choi, A. Berson, J.G. Pharoah, S.B. Beale, Part A J. Power Energy 225 (2011) 183—197.

[57] S. Jaganathan, B. Pourdeyhimi, H.V. Tafreshi, J. Eng. Fibers Fabr. 3 (2008).

[58] A. Nabovati, E.W. Llewellin, A.C.M. Sousa, Compos. Part A Appl. Sci. Manuf. 40 (2009) 860—869.

[59] V.D. Nguyen, E. Bchet, C. Geuzaine, L. Noels, Comput. Mater. Sci. 55 (2011) 390—406.

[60] H.G. Weller, G. Tabor, H. Jasak, C. Fureby, Comput. Phys. 12 (1998) 620—631.

[61] S.H. Chan, K.A. Khor, Z.T. Xia, J. Power Sources 93 (2001) 130—140.

[62] K. Tseronis, I.K. Kookos, C. Theodoropoulos, Chem. Eng. Sci. 63 (2008) 5626—5638.